Hybrid Plasma Simulations of Farley–Buneman Instabilities in the Auroral E–Region

E. L. Rojas[1], **D. L. Hysell**[1]

[1]Earth and Atmospheric Sciences, Cornell University

Key Points:

- Farley–Buneman simulations based on PIC are remarkably successful, but new approaches are needed to explore non-local processes.
- Hybrid continuous solvers are now an alternative when plasma structures are comparable to PIC numerical noise.
- Various aspects of Farley–Buneman instabilities were reproduced, with magnitudes comparable to experiments.

Corresponding author: Enrique Rojas, `elr96@cornell.edu`

Abstract

We implemented a hybrid continuous solver for fluid electrons and kinetic ions. Because the simulation is continuous, numerical noise is not an issue as it is for particle-in-cell approaches. Moreover, given that the ion kinetic equation is solved using a characteristic based method, no particle pushes have to be done. Our main goals are to reduce the computational cost of the simulations proposed by Kovalev (Kovalev, D.V. et al., 2008) and reproduce the main experimental features of Farley-Buneman instabilities measured by radars and rockets. The equations were derived from first principles using the approximations that are satisfied in the auroral E-region. Various tests will be presented to assess numerical accuracy. With the proposed numerical framework, we are able to recover important nonlinear features associated with Farley-Buneman instabilities: wave turning of dominant modes, and saturation of density irregularities at values consistent with experiments.

1 Introduction

Coupling between the magnetosphere and the high latitude ionosphere through energetic particles and electromagnetic fields results in the production of Hall currents that drive Farley–Buneman instabilities (Farley, D.T., 1963) which generate a spectrum of field–aligned plasma density irregularities (Rojas, E.L. et al., 2016). Numerous studies have shown that these irregularities can modify the mean state of the ionosphere through wave heating (St.Maurice, J.P., 1990), (Bahcivan, H., 2007). Furthermore, by affecting the local temperature several other parameters can also be modified: plasma density, composition, conductivity, and transport. Consequently, neutral wind surges, gravity waves, and traveling atmospheric and ionospheric disturbances can be produced which can ultimately affect ionospheric stability at lower latitudes (Fuller-Rowell, T.J. et al., 1994). Recently, studies have suggested that these instabilities can change the evolution of magnetospheric dynamics by changing the conductivity of the ionosphere (Wiltberger, M. et al., 2017).

Farley–Buneman waves belong to the family of two–stream instabilities. They develop at altitudes between 95 km and 120 km in the auroral and equatorial E region and to lesser extent at mid–latitudes (Sahr, J.D. & Fejer, 1996). In these regions, due to their different mobilities and collision rates, magnetized Hall–drifting electrons induce polarization drifts on the unmagnetized ions. Because of their inertia, ions tend overshoot the polarization field recovery and accumulate in the crests of the local density irregularities faster than diffusion opposes them (Hysell, D.L. et al., 2013). As a result, longitudinal density waves are formed. The propagation of these waves is nearly in the direction of the electron drifts, and their dominant wavelengths are in the order of few meters. In contrast to the equatorial case, in the auroral electrojet, wave heating plays an important role. Electric fields parallel and perpendicular (in lesser extent) to the background magnetic field have been shown to be important in explaining the heating observed in nature (Hysell, D.L., 2015). Moreover, these changes in temperature will influence the dynamics of the instabilities by changing some of the state parameters such as the ion–acoustic speed.

Linear, local fluid theory of Farley–Buneman instabilities, although limited, has produced some important, verified predictions. For instance, it gives a reasonable estimate for the threshold electric field (E_{th}) required to trigger the instabilities: the electron convection driven by this threshold fields has to be larger than the ion–acoustic speed to produce wave growth. Linear analysis of the full 5–moment system of equations has modified the initial estimates of E_{th} to take into account the role of thermal instabilities, which also produce a change in the direction of the waves (Dimant, Y.S. & Oppenheim, 2004). Although linear fluid theory predicts incorrectly the rapid growth of very short wavelengths, linear kinetic theory shows that ion Landau damping effectively suppresses this

growth (Schmidt, M.J. & Gary, 1973). Using these linear approximations, empirical models have been developed to interpret coherent radar backscatter and estimate local convection fields (Rojas, E.L. et al., 2018). Nevertheless, linear theory falls short in explaining several features observed in the experimental data (Oppenheim, M. et al., 1996). Most of the solutions of these problems cannot be expressed in closed form due to the strongly nonlinear behavior. Therefor, numerical simulations have to be implemented.

The first simulations of Farley–Buneman instabilities were based on a fluid plasma model (Newman, A.L. & Ott, 1981) with the inclusion of a wavelength dependent viscosity term as a proxy for Landau damping to avoid growth of small scale waves. Their simulation recovered wave turning effects. Shortly thereafter, Machida and Goertz (Machida, S. & Goertz, 1988) used a particle in cell (PIC) approach to model fully kinetic Farley–Buneman instabilities in a plane parallel to the magnetic field. Because of the geometry of the problem, the main source of nonlinearity for these irregularities was not included (Oppenheim, M. et al., 1996). Janhunen (Janhunen, P., 1994) also tried a fully kinetic PIC approach but modeled the instabilities in the direction perpendicular to B. Although these simulations did not achieve wave growth saturation (cessation of wave amplitude increase), some wave turning effects were seen.

The first numerical approaches were able to reproduce a number of experimental features of Farley–Buneman instabilities was developed by Oppenheim (Oppenheim, M. et al., 1996) using a hybrid (kinetic and fluid) model. Electrons were modeled as a fluid using the continuity and the inertialess momentum equation while ions evolved in phase space to preserve kinetic behavior. The kinetic evolution was performed using PIC integration, and the ion-neutral collisions were reproduced by a Monte Carlo approach. Quasineutrality was imposed by forcing the total current density to be solenoidal. This simulations were able to reproduce several experimental features: wave growth, secondary instabilities perpendicular to the electron flow, wave turning, and phase speed saturation close to the ion–acoustic speed. On time, Oppenheim extended this simulations first to a fully kinetic PIC approach (Oppenheim, M. & Dimant, 2004), then to a large–scale 2D simulation region of more than 100m (Oppenheim, M. et al., 2008), and finally to the full 3D case (Oppenheim, M. & Dimant, 2013).

Unfortunately, PIC simulations suffer from limitations that make them in some cases prohibitively expensive for studying non–local phenomena, especially when the full phase–space has to be considered. This is because PIC simulation noise decreases as $1/\sqrt{N}$, where N is the number of particles in each simulation cell. The implication of this restriction is that the number of particles required to have a significant signal to noise ratio will increase very rapidly with the size of the simulation box. Furthermore, the time integration of a system with a very large number of particles often requires the use of artificial particle masses and other nonphysical assumptions to decrease the computation time which complicates the final interpretation of the results.

In the past few years, several attempts have been made to simulate Farley–Buneman instabilities avoiding PIC approaches in order to create frameworks more suitable for non–local studies. Hassan (Hassan, E. et al., 2015) used a two–fluid simulation that included an additional stress term to emulate Landau damping, solving the continuity and momentum equation for both electron and ions species. However, Hammet (Hammett, G.W. & Perkins, 1990) has shown that a fluid Landau damping operator can be successfully constructed if higher moments are considered. More recently, Dolgov (Dolgov, S.V. et al., 2014) developed a hybrid fluid–electron kinetic–ion simulation and used a Tensor–Train format to reduce the dimensionality of the kinetic solver. Even though the memory reduction was significant, it is not yet clear to what extent in which the assumptions required for the Tensor-Train format affect the dynamics of the instabilities. Finally, Kovalev (Kovalev, D.V. et al., 2008) used also a hybrid fluid-kinetic approach, assuming isothermal electrons. In subsequent years thermal electrons were included by solving the full 5–moments electron equation (Kovalev, D.V. et al., 2009), but the final results seemed

to suggest that the energy equation did not fully reproduced the temperature evolution. This last approach employed a Semi–Lagrangian (SL) solver for the ions. The SL solver has gained increasing popularity in the plasma simulation community due to its locality, precision, simplicity, and the fact that it does not depend on the Courant–Friedrichs–Lewy (CFL) condition (Groppi, M. et al., 2016). These features make the SL solver a good candidate for studying the non–local behavior of Farley–Buneman instabilities.

In the present work, we implement a hybrid continuous solver for fluid electrons and kinetic ions using the SL method for the kinetic solver. Because the simulation is continuous, numerical noise is not an issue as it is in PIC approaches. Moreover, given that the SL solver is based on interpolation along the characteristics of the kinetic equation, no particle pushes (time integrations) have to be done. Our main goals are to reduce the computational cost of the simulations proposed by Kovalev and reproduce the main experimental features of Farley–Buneman instabilities obtained with radars and rockets. Although we are not going to address non–local phenomena in this work, we think that exploring these hybrid continuous strategies (even for small scale systems) is a necessary step in that direction.

The plasma models used in this simulation will be presented in the second section of the paper. The final form of the equations will be obtained from first principles using the approximations that are satisfied in the auroral E–region. In section three, the choice of numerical algorithms used to solve the model equations will be justified. Also, some benchmarks and tests will be presented in the appendix to assess the numerical accuracy of the algorithms. In section four, several simulations runs will be presented along with appropriate diagnostics. Section five will describe the main conclusions and future work.

2 Hybrid Plasma Model: Theory

Although the linear theory of Farley–Buneman instabilities has a limited set of verifiable predictions, it still can be used to identify the dominant processes and inform the choice of modeling equations for the hybrid solver. The linear, local dispersion relation of these waves can be written as (Farley, D.T., 2009):

$$\omega(k) = \frac{\boldsymbol{k}\cdot\boldsymbol{V}_d}{1+\psi} \tag{1}$$

$$\gamma(k) = \frac{\psi}{(1+\psi)\nu_{in}}(\omega^2(k)-k^2C_s^2)+\frac{\nu_{in}}{\Omega_i}\frac{\omega(k)k_E}{Lk^2}-2\alpha n_e, \tag{2}$$

where $\gamma(k)$ represents the growth rate for wave–number k, V_d is the electron advection speed, C_s the ion acoustic speed, α the dissociative recombination rate, n_e the electron density, L the scale length of density gradients, and

$$\psi(\theta) \approx \frac{\nu_{en}\nu_{in}}{\Omega_e\Omega_i}\left(1+\frac{\Omega_e^2}{\nu_{en}^2}\theta^2\right) \tag{3}$$

Here, $\Omega_{e,i}, \nu_{en,in}$ are the gyrofrequencies and neutral collision frequencies of electrons and ions, respectively. The angle θ indicates the complement of the angle between wave vector $\boldsymbol{k}$ and the magnetic field B ($\theta = 0$ corresponds to k perpendicular to B). k_E is the wave vector component in the direction of the background electric field.

Equation (2) has three terms corresponding to different contributions to wave growth. The first term measures the net effect between the destabilizing ion inertia and the stabilizing diffusion and is the one responsible for Farley–Buneman waves. The second and third terms correspond to the destabilizing or stabilizing effect of density gradients and the stabilizing effect of recombination, respectively. Moreover, the second term contributes to significant wave growth when $\nu_{in} \sim \Omega_i$ for wavelengths on the order of tens of meters (Fejer, B.G. et al., 1984). In the nonlinear regime, secondary waves are formed obliquely

to the primary wave by this same mechanisms. PIC simulations suggest that the coupling between these first and secondary waves is what cause the saturation of the wave growth (Oppenheim, M. et al., 2008).

Another important feature of equation (2) is its dependence on θ. In the auroral E region, the electrons are strongly magnetized ($\Omega_e \gg \nu_{en}$), which means that even small values of θ will give $\psi \gg 1$, making $\theta \approx 0$ the preferred direction for wave growth. This result is consistent with coherent scatter radar measurements, where echoes are observed roughly speaking from within 2 degrees of the plane perpendicular to B (Sahr, J.D. & Fejer, 1996). Nevertheless, it is important to mention that a significant number of experiments have consistently detected plasma fluctuations at much larger aspect angles. Several nonlinear mechanisms have been proposed to explain these large aspect angle fluctuations. Furthermore, there is evidence that waves parallel to B may be responsible for heating observed in incoherent scatter measurements (Bahcivan, H. & Cosgrove, 2010). When neglecting the last two terms in equation (2), it is evident that the highest growth will coincide with the smallest wavelengths. Schimdt (Schmidt, M.J. & Gary, 1973) showed that this non–physical growth rate was a limitation of the fluid dispersion relation and that including linear kinetic effects was enough to obtain realistic growth rates. They observed that Landau damping prohibited high wave number growth. Although both species experience Landau damping, electron damping is only effective at short wavelengths. Nevertheless, ion damping suppresses the oscillations at these short wavelengths. In other words, by resolving Landau damping with the ions, we make unnecessary the use of a kinetic model for the electrons. This of course assumes that Landau damping is the only kinetic process with a significant role in the evolution of Farley–Buneman instabilities.

Given that most of the dynamics occurs at small aspect angles, the model equations will be chosen to be two–dimensional, perpendicular to B. Also, in order to avoid contributions from gradient drift and recombination, the simulation sizes will be limited to less than 10 m. In summary, to prevent non–physical linear wave growth at small wavelengths, ions will be modeled kinetically.

2.1 Electric field model

Most ionospheric hybrid simulations enforce quasineutrality by constraining the total current density to satisfy $\nabla \cdot \boldsymbol{J} = 0$. We will not assume quasineutrality. Instead, to couple both species, we will solve Poisson's equation:

$$\nabla_\perp \cdot \delta \boldsymbol{E} = -\frac{e}{\varepsilon_0}(n_e - n_i) \tag{4}$$

As will become evident in section 3.1, the motivation for choosing to solve equation (4) is computational efficiency rather than the need to resolve deviations from quasineutrality.

2.2 Electron fluid model

Electrons will be modeled using an isothermal approximation of the simplified 5–moment transport equations in two dimensions, where only the perpendicular flow will be consider:

$$\frac{\partial n_e}{\partial t} + \nabla_\perp (n_e \boldsymbol{v}_{\perp e}) = 0 \tag{5}$$

$$\boldsymbol{v}_{\perp e} \nu_{en} m_e n_e = -\nabla_\perp p_e + e n_e (\boldsymbol{E}_\perp + \boldsymbol{v}_{\perp e} \times \boldsymbol{B}) + n_e m_e \boldsymbol{G}, \tag{6}$$

where e, p_e, m_e, n_e, and $\boldsymbol{v}_{\perp e}$ are the electron charge, pressure, mass, density, and fluid velocity perpendicular to B, respectively. Also, $\boldsymbol{E}_\perp$ is the total electric field perpendicular to B and $\boldsymbol{G}$ the acceleration due to gravity. Equation (6) is written in the frame

of reference of the neutral particles, in the plane perpendicular to B, and assuming inertialess electrons. Following (Schunk, R. & Nagy, 2009), neglecting the gravity and the diamagnetic drift, the electron velocity can be expressed explicitly as:

$$\boldsymbol{v}_{\perp e} = -\frac{kT_e}{m_e\nu_{en}p_e}\frac{1}{1+\Omega_e^2/\nu_{en}^2}\nabla_\perp p_e - \frac{e/(m_e\nu_{en})}{1+\Omega_e^2/\nu_{en}^2}\boldsymbol{E}_\perp + \frac{1}{B^2(1+\Omega_e^2/\nu_{en}^2)}\boldsymbol{E}_\perp \times \boldsymbol{B} \tag{7}$$

In this work, we assume that electrons are isothermal. Moreover, using the ideal gas approximation, $\nabla_\perp p_e = kT_e\nabla_\perp n_e$. The electric field can be decomposed such that $\boldsymbol{E}_\perp = \boldsymbol{E}_0 + \delta\boldsymbol{E}$, where $\boldsymbol{E}_0$ denotes the background electric field that account for the free energy source for the system and $\delta\boldsymbol{E}$ the electric field caused by density perturbations. Given that the electrons are strongly magnetized, $(1+\Omega_e^2/\nu_{en}^2)^{-1} \approx \nu_{en}^2/\Omega_e^2$. The convention chosen for the coordinate system will be as follows: the magnetic field $\boldsymbol{B} \parallel \hat{z}$, and $\boldsymbol{E}_0 \parallel \hat{y}$. Applying these approximations and conventions to equation (7) yields:

$$\boldsymbol{v}_{\perp e} = -\frac{kT_e\nu_{en}}{m_e\Omega_e^2 n_e}\nabla_\perp n_e - \frac{\nu_{en}e}{m_e\Omega_e^2}\delta\boldsymbol{E} - \frac{\nu_{en}e}{m_e\Omega_e^2}\boldsymbol{E}_0 + \boldsymbol{V}_0 + \frac{1}{B^2}\delta\boldsymbol{E}\times\boldsymbol{B}, \tag{8}$$

where $\boldsymbol{V}_0 = \boldsymbol{E}_0 \times \boldsymbol{B}/B^2$. In order to combine the momentum equation (8) with the electron continuity equation, the expression for $\nabla_\perp\cdot(n_e\boldsymbol{v}_{\perp e})$ has to be calculated. After some algebra, equation (5) can be written in the form of a diffusion-advection-reaction partial differential equation:

$$\frac{\partial n_e}{\partial t} + D_e\nabla_\perp^2 n_e + \boldsymbol{A}_e\cdot\nabla_\perp n_e + R_e n_e = 0, \tag{9}$$

where

$$D_e = -\frac{T_e}{e\kappa B} \tag{10}$$

$$A_{ex} = -\frac{1}{\kappa B}\delta E_x + \frac{1}{B}\delta E_y + V_0 \tag{11}$$

$$A_{ey} = -\frac{1}{\kappa B}\delta E_y - \frac{1}{B}\delta E_x - \frac{1}{\kappa B}E_0 \tag{12}$$

$$R_e = -\frac{1}{\kappa B}\nabla_\perp\cdot\delta\boldsymbol{E}, \tag{13}$$

and $\kappa = \Omega_e/\nu_{en}$ denotes the magnetization of electrons. Equation (9) is a second order linear partial differential equation. The reaction term R_e is proportional to $(n_e - n_i)$ and so is expected to be small. Because of the isothermal assumption, the diffusion term D_e will be constant. The advection term $\boldsymbol{A}_e$ will dominate equation (9). Furthermore, $\delta\boldsymbol{E}$ will increase due to the difference in mobility between electrons and ions in the $\hat{x}$ direction. Moreover, we can see how δE_x contributes to the advection perpendicular to the direction of the primary wave, setting the stage for secondary instabilities as expected from radar experiments.

2.3 Ion kinetic model

In order to resolve ion Landau damping, ions will have to evolve following the kinetic equation. If $f_i = f_i(\boldsymbol{x}, \boldsymbol{v}, t)$ is the ion distribution function in the phase–space, then:

$$\frac{\partial f_i}{\partial t} + \boldsymbol{v}_i\cdot\nabla f_i + \boldsymbol{a}_i\cdot\nabla_v f_i = J(f_i) \tag{14}$$

The acceleration $\boldsymbol{a}_i$ will be completely determined by the electric field because ions are not magnetized in the E–region. The operator ∇_v represents the gradient in velocity coordinates. The term on the right hand side corresponds to a general collision operator. Following the rationale established at the beginning of this section, we want to build a kinetic equation in the plane perpendicular to B. This can be achieved by neglecting $\hat{z}$

direction in configuration space. Assuming that the ion distribution in the $\hat{v}_z$ direction will be independent to the other directions, $f_i = n_i \hat{f}_{v_x,v_y} \hat{f}_{v_z}$, where the hat indicates a multivariate normal distribution. After replacing $\int f_i dv_z \rightarrow f_i$ and writing the acceleration explicitly we get:

$$\frac{\partial f_i}{\partial t} + \boldsymbol{v}_{\perp i} \cdot \nabla_\perp f_i + \frac{e}{m_i}(\boldsymbol{E}_0 + \delta \boldsymbol{E}) \cdot \nabla_{v\perp} f_i = J(f_i) \tag{15}$$

On the right hand side of (15), $J(f_i)$ is a general form collision operator that depends just on f_i.

The plasma in these regions is considered weakly ionized, and collisions are predominantly with neutral particles. Furthermore, according to (Dimant, Y.S. & Oppenheim, 2004), the time scale for the evolution of Farley–Buneman irregularities is given by $1/\nu_{in}$. This suggests that in order to reproduce a realistic time evolution, the kinetic collision operator should be adequate. Because of its complexity, the full Boltzmann collision operator will not be used in the present work. Instead, we will use the BGK ("Bhatnagar–Gross–Krook") operator to model ion–neutral collisions. This operator has the following form:

$$J(f_i) = -\nu_{in}(f_i - M[f_i]) \tag{16}$$

Here, $M[f_i]$ represents a drifting Maxwellian distribution defined by the velocity moments of f_i. It can be proven that this operator satisfies (Cercignani, C., 2012):

$$\int \alpha_k J(f_i) d^3v = 0 \tag{17}$$

$$\int \log f_i J(f_i) d^3v \leq 0, \tag{18}$$

where α_k represents the different velocity moments $\alpha_k = (1, m_i \boldsymbol{v}_i, m_i v_i^2/2)$. Equation (17) shows that the BGK operator conserves the first three moments locally by construction. The expression (18) is the Boltzmann inequality for the BGK operator, and it expresses the tendency of the plasma towards a Maxwellian distribution. Notice that the collision frequency is taken to be velocity independent. This approximation is appropriate for non–resonant ion–neutral collisions in the ionosphere (Schunk, R. & Nagy, 2009).

The final form of the ion kinetic equation is then:

$$\frac{\partial f_i}{\partial t} + \boldsymbol{v}_{\perp i} \cdot \nabla_\perp f_i + \frac{e}{m_i}(\boldsymbol{E}_0 + \delta \boldsymbol{E}) \cdot \nabla_{v\perp} f_i = -\nu_{in}(f_i - M[f_i]) \tag{19}$$

It is worth noting that equation (19) is strongly nonlinear, even more than for the case with the full Boltzmann collision operator. The main advantage of the chosen collision operator is that it is much easier to compute numerically (by estimating the velocity moments at each point in phase–space and constructing the corresponding Maxwellian distribution $M[f_i]$).

3 Hybrid Plasma Model: Numerics

In this section, the numerical algorithms to implement equations (4), (9), and (19) will be presented. Before going into the details of the solver, additional comments will be made about some numerically relevant physical features of Farley–Buneman instabilities. First, given the relatively small amplitude of these irregularities ($\delta n_e \approx 0.1 n_0$), we will assume that no significant shocks are going to be present. Furthermore, it can be argued that the quasi–linear structure of equation (9) does not indicate the presence of shocks in the electron density. Given that the electrons are dominated by advection, the characteristic curves will not intersect. The absence of shocks supports the use of spectral methods. Secondly, as mentioned before, the simulation size will be taken to be

on the order of 10 meters at maximum. Because no boundary effects are expected at these dimensions, we will assume periodic boundary conditions.

It is often convenient to decompose equations like (9) and (19) using the technique called operator splitting (Hundsdorfer, W. & Verwer, 2013). If an equation can be expressed as

$$\frac{\partial u}{\partial t} = (S_1 + S_2)u \tag{20}$$

then the analytical solution for a time Δt will be $u(t+\Delta t) = e^{\Delta t(S_1+S_2)}u(t)$. By constructing the corresponding series of the exponential operator, we can see that if the operators S_1 and S_2 commute, the solution can be written as $u(t+\Delta t) = e^{\Delta t S_1}e^{\Delta t S_2}u(t)$, which would be equivalent as solving the system

$$\frac{\partial u}{\partial t} = S_1 u \tag{21}$$

$$\frac{\partial u}{\partial t} = S_2 u \tag{22}$$

and using the solution of (21) as the initial condition of (22) instead of solving the more complicated (20) without any numerical error caused by the splitting. If the operators do not commute, the global numerical error will be of the order of $\mathcal{O}(\Delta t)$. In this case, the error can be diminished using Strang splitting (Strang, G., 1968) instead, in which case the solution would be expressed as $u(t+\Delta t) = e^{\frac{\Delta t}{2}S_1}e^{\Delta t S_2}e^{\frac{\Delta t}{2}S_1}u(t)$. Using Strang splitting, the global error will be of the order of $\mathcal{O}(\Delta t^2)$. Furthermore, this approach can be extended for an arbitrary number of operators, such that if

$$\frac{\partial u}{\partial t} = (S_1 + \ldots + S_n)u \tag{23}$$

then,

$$u(t+\Delta t) = e^{\frac{\Delta t}{2}S_1}\ldots e^{\frac{\Delta t}{2}S_{n-1}}e^{\Delta t S_n}e^{\frac{\Delta t}{2}S_{n-1}}\ldots e^{\frac{\Delta t}{2}S_1}u(t) \tag{24}$$

keeping the global error at $\mathcal{O}(\Delta t^2)$. This means that equation (23) can be solved with second order precision in time by solving for each operator S_i and using as the initial condition the solution of the equation corresponding to the operator S_{i-1}. Higher order splitting methods have been developed, but they are significantly more expensive to implement. We will use this second order splitting because it provides a good balance between complexity and precision (Glowinski, R. et al., 2017).

3.1 Electric field solver

As mentioned at the beginning of this section, given that shocks are not expected and periodic boundary conditions are imposed, a spectral collocation method for the electric field solver is justified. Writing (4) in terms of the electric potential ϕ and δn and taking the Fourier transform at both sides:

$$\nabla^2\phi = \frac{e}{\varepsilon_0}\delta n \rightarrow -|\boldsymbol{k}|^2\tilde{\phi} = \frac{e}{\varepsilon_0}\delta\tilde{n} \tag{25}$$

$$\Rightarrow \quad \delta\tilde{\boldsymbol{E}} = -i\frac{e\delta\tilde{n}}{|\boldsymbol{k}|^2}\boldsymbol{k}, \tag{26}$$

where $\delta\tilde{\boldsymbol{E}} = -i\boldsymbol{k}\phi$ and the tilde indicates the Fourier transformed function. The electric field can be recovered by applying the inverse Fourier transform to (26). The periodic bounds cause each wave component to be zero when integrated over the whole domain. The exception is the component corresponding to the zero wave–number which will be a constant. Consequently, to enforce periodic bounds, we will make $\tilde{\phi}(0,0) = 0$ in equation (25). The full calculation of the perturbed electric field can be described with

the algorithm EFieldSolve described in Figure 1. Notice that $\mathcal{F}$, and $\mathcal{F}^{-1}$ denote the Fourier transform and its inverse, respectively. However, given that this procedure does not include de–aliasing, the solver precision will be affected when higher wavenumbers components start increasing.

Algorithm Electric Field Solver

procedure EFieldSolve(n_e, n_i)
  $\tilde{\phi}(k_x, k_y) = -\frac{e}{\varepsilon_0 |\boldsymbol{k}|^2} \mathcal{F}\{n_e - n_i\}$
  $\tilde{\phi}(0,0) = 0$
  $\delta \boldsymbol{E} = \mathcal{F}^{-1}\{-i\boldsymbol{k}\tilde{\phi}\}$ ▷ Keeping just real part
  return $\delta \boldsymbol{E}$

Figure 1. Numerical algorithm for the solution of Poisson equation.

3.2 Electron fluid solver

There are two fundamental reasons to split equation (9). First, we see that the diffusion term has a constant diffusion coefficient which means that it can be solved efficiently with a Fourier spectral collocation method (Hesthaven, J.S., 2017), and the reaction term is simple enough to be solved analytically. Secondly, by isolating the advection term, we can use a characteristic–based method. Even though it is possible to extend the diffusion equation to include the reaction term as a heat source in order to have just one splitting, this will not be a significant advantage because the algorithm would still be of second order. Moreover, the computational cost of adding an extra step for the reaction term is minimal as will be shown.

We can rewrite the electron evolution equation as

$$\frac{\partial n_e}{\partial t} = (S_\mathrm{D} + S_\mathrm{A} + S_\mathrm{R}) n_e \tag{27}$$

where S_D, S_A,and S_R correspond to the diffusion, advection, and reaction operators, respectively. In order to define the decomposition of equation (9), we first have to verify whether the operators commute. As proven by (Lanser, D. & Verwer, 1999), $[S_\mathrm{D}, S_\mathrm{A}] = 0$ when D_e and $\boldsymbol{A}_e$ are position independent, $[S_\mathrm{A}, S_\mathrm{R}] = 0$ when $\nabla \cdot \boldsymbol{A}_e = 0$ and R_e is position independent, and $[S_\mathrm{D}, S_\mathrm{R}] = 0$ when R_e is linear in n_e and position independent. As we can see from the definitions of D_e, $\boldsymbol{A}_e$, and R_e, none of the commutation conditions are satisfied. Consequently, the time evolution of equation (9) in terms of Strang splitting will be:

$$n_e(x, y, t + \Delta t) = e^{\frac{\Delta t}{2} S_\mathrm{D}} e^{\frac{\Delta t}{2} S_\mathrm{R}} e^{\Delta t S_\mathrm{A}} e^{\frac{\Delta t}{2} S_\mathrm{R}} e^{\frac{\Delta t}{2} S_\mathrm{D}} n_e(x, y, t) \tag{28}$$

An intuitive way to understand equations (9) and (28) is the following: the electron density wave modes are damped at a rate D_e, the density perturbations are amplified by the charge separation, and constant parcels of density are transported along $\boldsymbol{A}_e$.

The diffusion step

$$\frac{\partial n_e}{\partial t} = S_\mathrm{D} n_e = -D_e \nabla^2 n_e \tag{29}$$

can be solved with a spectral collocation method using the Fourier basis, as indicated before. Taking the spatial Fourier transform at both sides of (29) gives

$$\frac{\partial \tilde{n}_e}{\partial t} = i D_e |\boldsymbol{k}|^2 \tilde{n}_e, \tag{30}$$

where $\tilde{n}_e(\boldsymbol{k}, t)$ is the spatial Fourier transform of the electron density. Integrating (30) over a time step Δt and applying the inverse Fourier transform to go back to physical space will results in the solution of (29).We can write the full solution of the diffusion step as

$$n_e(t + \Delta t) = \mathcal{F}^{-1}\{e^{iD_e|\boldsymbol{k}|^2\Delta t}\mathcal{F}\{n_e(t)\}\} \tag{31}$$

Because there is no interaction between modes, and we are using periodic boundary conditions, no further corrections need to be made to this approximation. Furthermore, the precision and speed of this estimate will be determined by the precision and speed of the fast Fourier transform function used. The reaction step

$$\frac{\partial n_e}{\partial t} = S_{\mathrm{R}} n_e = -R_e n_e \tag{32}$$

can be solved by directly integrating over a time step Δt because although R_e depends on the time evolution of the electric field, at each split term, the electric field can be considered constant in time. Therefor, the reaction step can be written as

$$n_e(t + \Delta t) = e^{-R_e \Delta t} n_e(t) \tag{33}$$

Even though $-R_e > 0$, because is very small, the amplification caused by this term is almost negligible even if there is a significant charge separation. Finally, the advection step

$$\frac{\partial n_e}{\partial t} = S_{\mathrm{A}} n_e = \boldsymbol{A}_e \cdot \nabla n_e \tag{34}$$

can be solved using the method of characteristics (Hesthaven, J.S., 2017). Therefor, if (x^*, y^*) is a point in the characteristics of (34) corresponding to a time step backwards in time, then the density can be expressed as $n_e(x, y, t) = n_e(x^*, y^*, t - \Delta t)$. Defining $s_x = x - x^*$ and $s_y = y - y^*$, we can use the recursion proposed be (Robert, 1981) to estimate (x^*, y^*):

$$\boldsymbol{s}^{(k+1)} = \Delta t \boldsymbol{A}_e(\boldsymbol{r} - \boldsymbol{s}^{(k)}\Delta t) \tag{35}$$

Notice that this is only necessary because the advection field is position dependent. Once $\boldsymbol{s}$ is calculated for each grid point, we can integrate (34) a time Δt:

$$n_e(x, y, t + \Delta t) = n_e(x - s_x(x, y), y - s_y(x, y), t) \tag{36}$$

Clearly, the points $(x - s_x(x, y), y - s_y(x, y))$ will not in general be defined on the grid points, but the values of n_e on these coordinates can be estimated with interpolation methods. This approach is called semi–Lagrangian because it solves the equation along the characteristics but in an eulerian reference frame. We use a cubic spline interpolation because it has been shown to perform better than high order polynomial interpolation and it preserves the continuity of the first and second derivatives by construction. If g is a one dimensional function and s_3 is its cubic spline representation, it can be shown (Quarteroni, A. & Valli, 2008) that

$$|g - s_3| \leq \frac{5}{384} h^4 \max\{g^{(4)}\} \tag{37}$$

, where $g^{(4)}$ denotes the fourth derivative of g and h the width of the domain's partition, which implies that the spline error is $\mathcal{O}(h^4)$. In Figure 2 we see explicitly the numerical algorithm proposed to solve (9). It is important to notice that R_e and $\boldsymbol{A}_e$ are calculated with the density values at each split step. As we will see in section 3.4, the electron solver runs several iterations before the ion step. By recognizing that $[S_{\mathrm{D}}, S_{\mathrm{D}}] = 0$ and using equation (28), we can group together adjacent diffusion steps from consecutive iterations. For instance, with just two electron evolution steps:

$$\begin{aligned} n_e(x, y, t + 2\Delta t) &= e^{\frac{\Delta t}{2} S_{\mathrm{D}}} e^{\frac{\Delta t}{2} S_{\mathrm{R}}} e^{\Delta t S_{\mathrm{A}}} e^{\frac{\Delta t}{2} S_{\mathrm{R}}} e^{\frac{\Delta t}{2} S_{\mathrm{D}}} e^{\frac{\Delta t}{2} S_{\mathrm{D}}} e^{\frac{\Delta t}{2} S_{\mathrm{R}}} e^{\Delta t S_{\mathrm{A}}} e^{\frac{\Delta t}{2} S_{\mathrm{R}}} e^{\frac{\Delta t}{2} S_{\mathrm{D}}} n_e(x, y, t) \\ &= e^{\frac{\Delta t}{2} S_{\mathrm{D}}} e^{\frac{\Delta t}{2} S_{\mathrm{R}}} e^{\Delta t S_{\mathrm{A}}} e^{\frac{\Delta t}{2} S_{\mathrm{R}}} e^{\Delta t S_{\mathrm{D}}} e^{\frac{\Delta t}{2} S_{\mathrm{R}}} e^{\Delta t S_{\mathrm{A}}} e^{\frac{\Delta t}{2} S_{\mathrm{R}}} e^{\frac{\Delta t}{2} S_{\mathrm{D}}} n_e(x, y, t) \end{aligned} \tag{38}$$

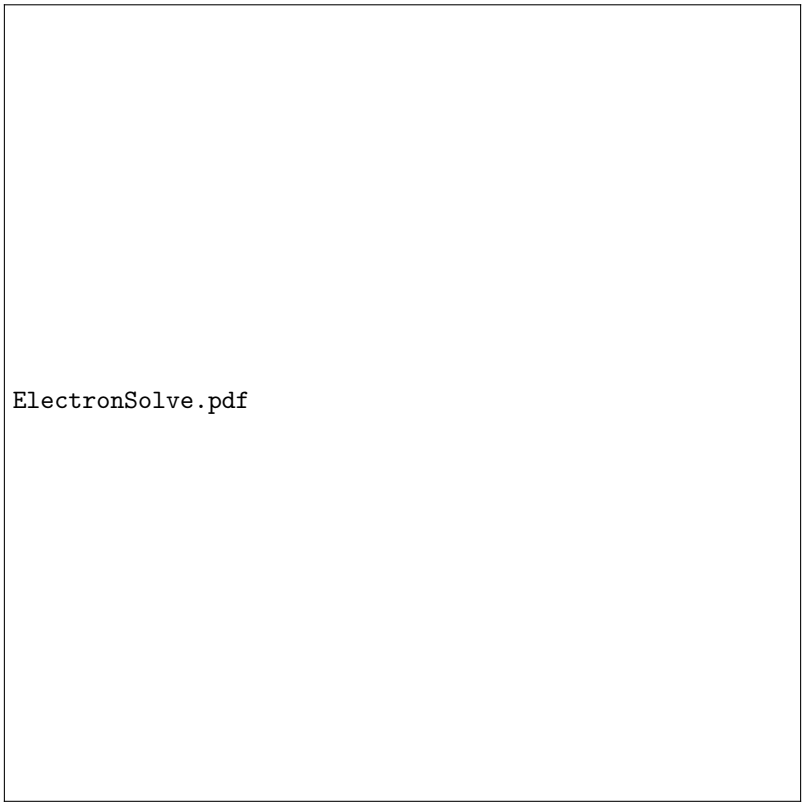

Figure 2. Numerical algorithm for the evolution of electrons a time $r_t \Delta t_e$.

The inner loop starting at line 3 makes the electron evolve a number r_t of times. If Δt_e and Δt_i are the electron and ion time steps, respectively, then $r_t = \Delta t_i / \Delta t_e$. The conditional of line 13 activates only at the last iteration, which corresponds to the last diffusion half step as seen in equation (38). Following (Robert, 1981) approach, the recursion of line 9 iterates three times. The fluid model was split to avoid nonlinearities, so each fractional step is approximately linear and periodic. Although the splitting is second order, because the electric field is not being calculated at fractional time steps but is assumed constant, the fluid time step will be affected. As the electric deviates from constant, the second order accuracy will move to first order.

3.3 Ion kinetic solver

The kinetic equation (19) has the form of a advection–reaction equation in a 5D phase–space. We will solve (19) using the semi–Lagrangian approach as described by (Cheng, C. & Knorr, 1976) and (Filbet, F. et al., 2001). There is a vast literature on semi–Lagrangian methods for the electrostatic and the electromagnetic Vlasov equation. Various numerical experiments have shown that semi–Lagrangian methods outperform spectral, finite diference, and finite volume methods in reproducing streaming instabilities and Landau damping (Sonnendrücker, E. et al., 1999). Furthermore, these tests suggested that the results obtained with spline interpolation are comparable to ninth–order polyniomial interpolation. However, general spline interpolation does not have any positivity constraints which are needed for the distribution function. Moreover, spurious diffusive oscillations are known to occur under polynomial interpolation. Some strategies to overcome these difficulties have been proposed, for instance, WENO ("Weighted essentially non–oscillatory")

interpolation methods (Qiu, J. & Christlieb, 2010). These new strategies are subjects of future work.

Following the approach of the previous section, we can express the ion evolution equation as:

$$\frac{\partial f_i}{\partial t} = (S_{\mathrm{A}_r} + S_{\mathrm{A}_v} + S_{\mathrm{BGK}})f_i, \tag{39}$$

where S_{A_r} and S_{A_v} correspond to the advection in the (x, y) plane and the (v_x, v_y) plane, respectively. Operator S_{BGK} represents the reaction term corresponding to the BGK operator. Note that the splitting in this case is different from the electron case. For instance, the advection term is split by dimension and not by operator type. Furthermore, the BGK operator is significantly more complex than the electron reaction term because it contains several integrals over velocity space for the calculation of moments. This makes equation (39) very nonlinear but significantly easier to solve numerically than the full Boltzmann equation. As for the electron case, in order to determine the appropriate operator decomposition, the commuting properties of the operators in equation (39) have to be evaluated. The commutators to calculate are $[S_{\mathrm{A}_r}, S_{\mathrm{A}_v}]$, $[S_{\mathrm{A}_v}, S_{\mathrm{BGK}}]$, and $[S_{\mathrm{BGK}}, S_{\mathrm{A}_r}]$. The two advection operators do not commute because of the electric field dependence on position, and the BGK operator term does not commute with any of the advection terms because it also depends on position. Therefor, Strang splitting is required to preserve the second order precision in time:

$$f_i(x, y, v_x, v_y, t + \Delta t) = e^{\frac{\Delta t}{2} S_{\mathrm{BGK}}} e^{\frac{\Delta t}{2} S_{\mathrm{A}_r}} e^{\Delta t S_{\mathrm{A}_v}} e^{\frac{\Delta t}{2} S_{\mathrm{A}_r}} e^{\frac{\Delta t}{2} S_{\mathrm{BGK}}} f_i(x, y, v_x, v_y, t) \tag{40}$$

This splitting, without taking into account the collision term, was proposed first by (Cheng, C. & Knorr, 1976). An intuitive way to understand equations (19) and (40) is as follows: the BGK operator changes the local distribution to a Maxwellian at a rate ν_{in}, constant parcels of f_i are transported along lines of constant velocity and constant acceleration.

The collision step

$$\frac{\partial f_i}{\partial t} = S_{\mathrm{BGK}} f_i = -\nu_{in}(f_i - M[f_i]) \tag{41}$$

can be solved analytically, because the maxwellian $M[f_i]$ is determined by the ion moments $(n_i, \boldsymbol{u}_i, T_i)$ at each instant of time for each point in phase space. All the moments can be obtained from the following relations:

$$\begin{aligned} (n_i, n_i \boldsymbol{u}_i, E_i)^T &= \int \left(1, \boldsymbol{v}_i, \frac{|\boldsymbol{v}_i|^2}{2}\right)^T f_i d^3 v_i \\ E_i &= \frac{n_i u_i^2}{2} + \frac{n_i k T_i}{2}, \end{aligned} \tag{42}$$

where E_i is the ion kinetic energy per unit mass, and the $\perp$ symbol has been dropped from the ion velocity. After defining the corresponding maxwellian, equation (41) can be integrated a time Δt (Liboff, R.L., 2003):

$$f_i(\boldsymbol{r}_i, \boldsymbol{v}_i, t + \Delta t) = f_i(\boldsymbol{r}_i, \boldsymbol{v}_i, t) e^{-\nu_{in} \Delta t} + M[f_i(\boldsymbol{r}_i, \boldsymbol{v}_i, t)](1 - e^{-\nu_{in} \Delta t}) \tag{43}$$

The advection steps in the (x, y) and (v_x, v_y) planes:

$$\frac{\partial f_i}{\partial t} = S_{\mathrm{A}_r} f_i = -\boldsymbol{v}_i \cdot \nabla f_i \tag{44}$$

$$\frac{\partial f_i}{\partial t} = S_{\mathrm{A}_v} f_i = -\frac{e}{m_i}(\boldsymbol{E}_0 + \delta \boldsymbol{E}) \cdot \nabla_v f_i \tag{45}$$

can be solved using the semi–Lagrangian method presented before. In this case, we see that the interpolations can used in the (x, y) and (v_x, v_y) planes assuming that the velocity and position are constant, respectively for each fractional step. Equations (44) and

(45) can then be integrated a time Δt by:

$$f_i(\boldsymbol{r}_i, \boldsymbol{v}_i, t + \Delta t) = f_i(\boldsymbol{r}_i - \boldsymbol{v}_i \Delta t, \boldsymbol{v}_i, t) \quad (46)$$

$$f_i(\boldsymbol{r}_i, \boldsymbol{v}_i, t + \Delta t) = f_i(\boldsymbol{r}_i, \boldsymbol{v}_i - \frac{e}{m_i}(\boldsymbol{E}_0 + \delta \boldsymbol{E})\Delta t, t), \quad (47)$$

respectively. Notice that in (46), the shifting of the grid will not change as the system evolves because v_i are the grid values in the v_x, v_y plane and will be defined when the system is initialized. On the other hand, to interpolate (47), $\delta \boldsymbol{E}$ will have to be calculated at each new time iteration, which involves the calculation of the zeroth moment. Equations (46) and (47) are by far the most computationally demanding of this simulation. For instance, if the velocity grid has a size of $N_v \times N_v$ and the position grid a size of $N_r \times N_r$, equation (46) will involve N_v^2 interpolations on a N_r^2 grid and equation (47) N_r^2 interpolations on a N_v^2 grid. This step is analogous to the particle push in PIC simulations.

Algorithm Ion Kinetic Solver

1: **procedure** IONSOLVE($n_e, f_i, \Delta t_i$)
2: $(n_i, n_i \boldsymbol{u}_i, E_i) \leftarrow \sum_{-v_{\max}}^{v_{\max}} \left(1, \boldsymbol{v}_i, \frac{|\boldsymbol{v}_i|^2}{2}\right) f_i \Delta v_i^2$
3: $T_i \leftarrow \frac{1}{k}(\frac{2E_i}{n_i} - |\boldsymbol{u}_i|^2)$
4: Map $M[f_i]$ with $(n_i, \boldsymbol{u}_i, T_i)$
5: $f_i \leftarrow f_i e^{-\nu_{in}\Delta t/2} + M[f_i](1 - e^{-\nu_{in}\Delta t/2})$
6: **for** $(v_{x_\alpha}, v_{y_\beta})$ where $(\alpha, \beta) \in [1, N_v] \times [1, N_v]$ **do**
7: $(x^*, y^*) \leftarrow (x - v_{x_\alpha}\Delta t_i/2, y - v_{y_\beta}\Delta t_i/2)$
8: $f_i(x, y) \leftarrow f_i(x^*, y^*)$
9: $n_i \leftarrow \sum_{-v_{\max}}^{v_{\max}} f_i \Delta v^2$
10: $\delta \boldsymbol{E} \leftarrow$ EFIELDSOLVE(n_e, n_i)
11: **for** (x_α, y_β) where $(\alpha, \beta) \in [1, N_r] \times [1, N_r]$ **do**
12: $(v_x^*, v_y^*) \leftarrow (v_x - \frac{e}{m_i}\delta E_x \Delta t_i, v_y - \frac{e}{m_i}(E_0 + \delta E_y)\Delta t_i)$
13: $f_i(v_x, v_y) \leftarrow f_i(v_x^*, v_y^*)$
14: **for** $(v_{x_\alpha}, v_{y_\beta})$ where $(\alpha, \beta) \in [1, N_v] \times [1, N_v]$ **do**
15: $(x^*, y^*) \leftarrow (x - v_{x_\alpha}\Delta t_i/2, y - v_{y_\beta}\Delta t_i/2)$
16: $f_i(x, y) \leftarrow f_i(x^*, y^*)$
17: $(n_i, n_i \boldsymbol{u}_i, E_i) \leftarrow \sum_{-v_{\max}}^{v_{\max}} \left(1, \boldsymbol{v}_i, \frac{|\boldsymbol{v}_i|^2}{2}\right) f_i \Delta v_i^2$
18: $T_i \leftarrow \frac{1}{k}(\frac{2E_i}{n_i} - |\boldsymbol{u}_i|^2)$
19: Map $M[f_i]$ with $(n_i, \boldsymbol{u}_i, T_i)$
20: $f_i \leftarrow f_i e^{-\nu_{in}\Delta t/2} + M[f_i](1 - e^{-\nu_{in}\Delta t/2})$
21: **return** f_i

Figure 3. Numerical algorithm for the evolution of ions a time Δt_i

Figure 3 shows the numerical algorithm for the evolution of ions. Lines 2-5 and 17-20 correspond to the collision steps, the rest are for the advection in configuration and velocity space. Note that in line 10 the perturbed electric field has to be recalculated with the updated values of f_i. In contrast to the electron case, here the characteristic curves can be taken as constant on each fractional step, which obviates the need to use the recursion (35).

3.4 Building the hybrid solver and diagnostics

Now that each solver has been described, we can construct the final form of the hybrid solver. Given that charge mobility is inversely proportional to the mass, we see that for the E region context, electron mobility is much higher than ion mobility. This difference in mobility allows the solver to have $\Delta t_i > \Delta t_e$. Consequently, r_t can have relatively high values. We can construct the hybrid solver using the previously described

algorithms as shown in Figure (4). The present method differs from the one used in (Kovalev, D.V. et al., 2008) in two fundamental ways. First, they used an alternate-direction implicit method for the fluid electrons, and second, they solved the kinetic system by a modified semi-Lagrangian interpolation that includes the collision term. The electron density was initialized by simulating a pink noise distributed perturbation (δn) of the background plasma density (n_0), such that $n_e(x, y, t = 0) = n_0(1 + \delta n)$ (Figure 5). The amplitude of the perturbation was chosen to be on the order of 0.1% of the background density. The ion distribution function was initialized by using the same charge distribution of the electrons ($n_i(x, y, t = 0) = n_e(x, y, t = 0)$) and a Maxwellian velocity distribution centered at the origin (Figure 5). The chosen coordinate system is illustrated in Figure 5, with earth's magnetic field B in the direction perpendicular to the plane, the background electric field $\boldsymbol{E}_0 \parallel \hat{y}$ and $V_0 \parallel \boldsymbol{E}_0 \times \boldsymbol{B} \parallel \hat{x}$. Given that two consecutive electron $\Delta t/2$ time steps commute, using a second order splitting to evolve both species will be equivalent to do consecutive Δt steps as long as the first step is $\Delta t/2$. These approximations will be tested in future work through scaling studies.

Algorithm Hybrid Solver

```
Pink noise δn
n_e, n_i ← n_0(1 + δn)
f_i initialized as Maxwellian
for i = 1 : N_steps do
    n_e ← ElectronSolve(n_e, ni, Δt_e, r_t)
    f_i ← IonSolve(n_e, f_i, Δt_i)
    if (i mod N_sample) = 0 then                ▷ Perform diagnosis
        Collect E_rms, < δn^2 >
        Collect ñ_e(k, ω)
Write to file
```

Figure 4. Numerical algorithm for the Hybrid Solver proposed in this work to study Farley–Buneman instabilities.

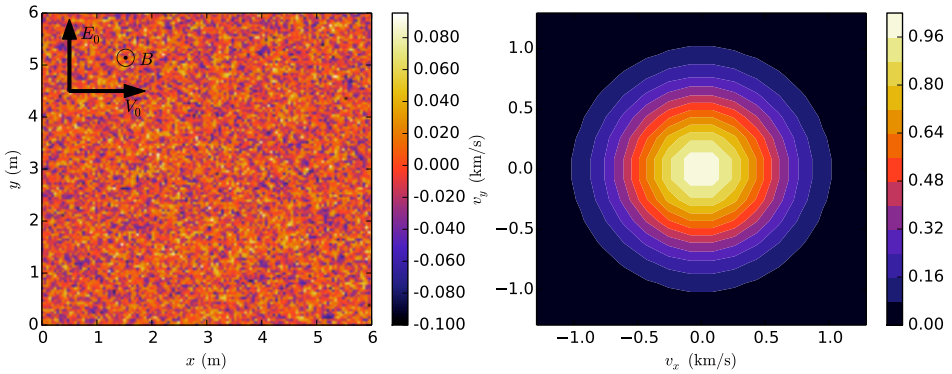

Figure 5. *Left:* Initial $\delta n/n_0$ distribution generated with attenuated noise ($\propto 1/|\boldsymbol{k}|^{1/2}$).*Right:* Integrated initial ion distribution function over all configuration space and selecting a sub interval of the full velocity domain.

As we can see in Figure 4, the diagnostic block will retrieve from the solver several important variables every N_{steps} iterations. These time series will be constructed

in the same way as has been presented in most of the literature. The root mean square (rms) electric field E_{RMS} estimate will be calculated from just the perturbed electric field, in other words, using $\delta \boldsymbol{E}$ without considering $\boldsymbol{E}_0$. For measuring the nonlinear wave growth, we will calculate the standard deviation of the perturbed component of the density $\delta n = n_e/n_0 - 1$. The other component of the diagnostic section is the spectral analysis of the density perturbations, which will focus on the monitoring of the relative power and the phase speed of different wave k-modes. By calculating the spatial Fourier transform $\tilde{n}_e(\boldsymbol{k}, t) = \mathcal{F}\{n_e(\boldsymbol{r}, t)\}$, we can visualize how the wave modes are distributed by plotting the normalized power spectral density.

It is worth noting that N_{steps} has to be large enough to sample at times that are on the order of magnitude of the period of the density irregularities.

4 Simulation Runs and Discussion

In this section, we will use the numerical algorithms designed in section 3 to solve equations (9), (19), and (4). These equations capture the relevant physics of Farley–Buneman instabilities. The coefficients for this system of equations will be calculated using the parameters from Table (1). The simulation will be initialized as described in section 3.4. The background electric field E_0 is well above the threshold for instability (≈ 20 mV/m), according linear theory. Notice that the coarse discretization of the velocity space will affect how well Landau damping is resolved. The impact of the velocity resolution on the simulation results will be a topic of future work. All the tests presented in this work were done on a laptop (Intel core i5 and 4GB of RAM) and took between 2 a 4 hours to run.

Table 1. Simulation parameters

Name	Symbol	Value
Background Electric field	E_0	50 mV/m
Background Magnetic field	B_0	5×10^{-5}T
Ion–neutral collision frequency	ν_{in}	2.5×10^{3}Hz
Electron and Ion temperatures	$T_e = T_i$	300K
Plasma density	N_0	$10^{10}\mathrm{m}^{-3}$
Ion time step	Δt_i	5×10^{-6}s
Number of grid points in each dimension	N_x, N_v	256,32
Lateral size of simulation box	L	3m
Ion Velocity range	$[-6v_{th}, 6v_{th}]$	$[-1.75, 1.75]$km/s
Ratio $\Delta t_i/\Delta t_e$	r_t	10

Figure (6) illustrates the early stages of wave growth. Each row corresponds to a different time iteration. The first column shows the perturbed electron density $\delta n_e = n_e/n_0 - 1$. The second column shows the root mean square values of $\delta \boldsymbol{E}$ and of δn_e relative to the background n_0. These two metrics are widely used in the literature because they capture important signatures of nonlinear dynamics. The dashed black line indicates the value of the background electric field. In the third column, we show the normalized power spectra $|\tilde{n}_e(k_x, k_y)|$ for the corresponding density distribution which provide information about the dominant wave modes.

The first row of Figure (6) represents the system a few iterations after initialization. We see that $|\delta n_e| < 0.01$ and is not yet resolvable with the scale used. This also can be seen in the adjacent plot, where the perturbations in the electric field are still very small. Likewise, the power spectra shows a broad energy distribution across many wave

modes which are the remnants of the white noise used for initialization. Its vertical and horizontal axis correspond to the the λ_y and λ_x waves modes. In the second, row we show the system after 7,000 ion time steps. The density perturbations are now $\delta n_e < 0.05$ and show a well defined wave–like structure. As expected from linear theory, we see that the root mean square of δn_e follows an exponential increase. The power spectra is now concentrated in a few oblique modes and shows a clear deviation from the $E_0 \times B_0 \parallel x$ direction. Moreover, large wavelength modes perpendicular to $E_0 \times B_0$ started to form around the origin which corresponds to the perpendicular secondary waves driven by the y component of $\delta \boldsymbol{E}$.

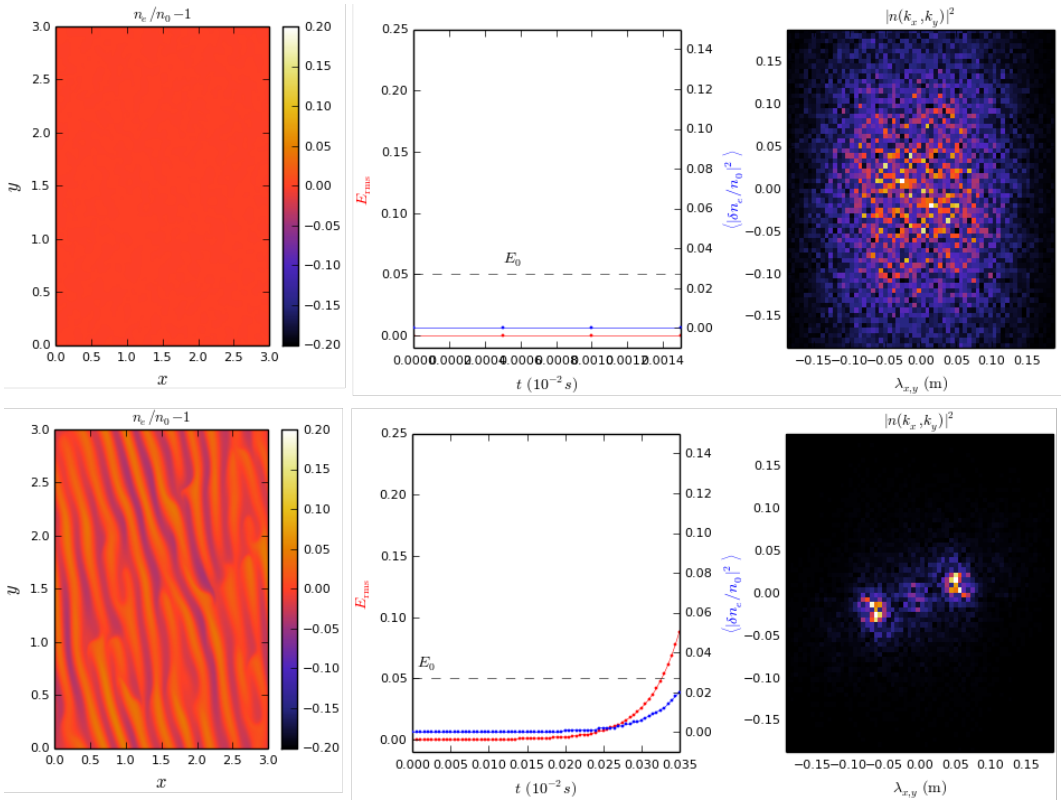

Figure 6. Evolution of δn_e and $\delta \boldsymbol{E}$. *Right:* Density perturbations. *Middle:* Root mean square of time series of δn_e and $\delta \boldsymbol{E}$. *Left:* Normalized $|\tilde{n}(k_x, k_y)|$. *Top:* 300 ion time steps. *Bottom:* 7000 ion time steps.

Figure (7) represents the system close to and after the amplitude saturates. In the first row, we see the system after 8500 ion time steps. The density irregularities are clearly propagating at an angle different to the x direction, and their amplitude is $\delta n_e < 0.1$. Furthermore, we can clearly see irregularities forming in the vertical direction. The amplitude of the density irregularities is still increasing exponentially. The root mean square electric field has increased to be much larger than E_0, which contradicts the results from PIC simulations and rocket in–situ measurements. These runs were stopped when $E_{rms} \approx 10E_0$. The power spectra show that the wave modes surrounding the origin in the previous plot have now coupled together with the primary waves. Furthermore, we see that the wave modes have clustered between the axis, which suggest a tilt in the main modes of wave propagation with respect to the $E \times B$ direction. This wave turning effect is consistent with previous PIC simulations and radar experiments. The system presented in the second row has evolved for 9,700 ion time steps. The rms peak of δn_e indicates

saturation which means that the system is now dominated by the strongly nonlinear $\delta \boldsymbol{E}$. Both the power spectra and the density plots show that formation of small scale wave modes after saturation.

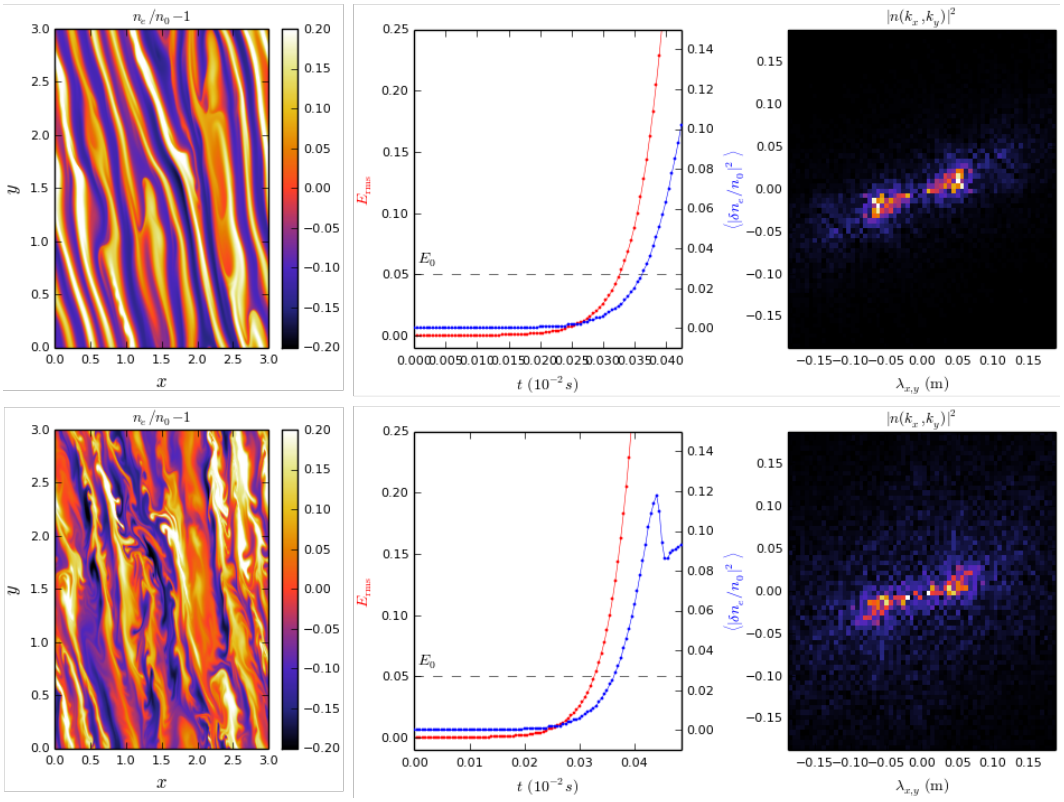

Figure 7. Evolution of δn_e and $\delta \boldsymbol{E}$. *Top:* 8500 ion time steps. *Bottom:* 9700 ion time steps.

A second run was made using almost the same simulation parameters from Table (1), using new values for $\Delta t_i = 2 \times 10^{-5} s$, $E_0 = 80 mV/m$, and $r_t = 20$. The rest of features of this second run are the same as the first one.

Figures (8) and (9) correspond to the second run, and show the density perturbations at three different times and the temporal evolution of δE_{RMS} and the root mean square of the irregularities, respectively. Notice that each density plot is label with a letter that is located at its corresponding location in the time series of Figure (9).

The first density plot (**A**) was taken after 1400 ion time steps when the exponential wave growth is occurring. Because the background electric field used for this run is larger than the one used in the previous run but the threshold for instability is the same, wave growth starts sooner. The second density plot (**B**) was taken after 1800 ion time steps, just before the system saturates. After saturation, we see that the irregularities fluctuate around $0.7 n_0$, consistent with rocket measurements (Sahr, J.D. & Fejer, 1996). In this run, we see that the electric field saturates at values much closer to E_0, a behavior better aligned with the experimental evidence (Sahr, J.D. & Fejer, 1996; Bahcivan, H. et al., 2006). The last plot (**C**) illustrates the density irregularities after 3600 ion steps. Although the temporal evolution of the irregularities is more stable in this run, we see that small scale structures emerged after saturation that were not present in the previous run. These small scale structures are not present in PIC simulations of Farley–Buneman instabilities (Oppenheim, M. et al., 1996, 2008).

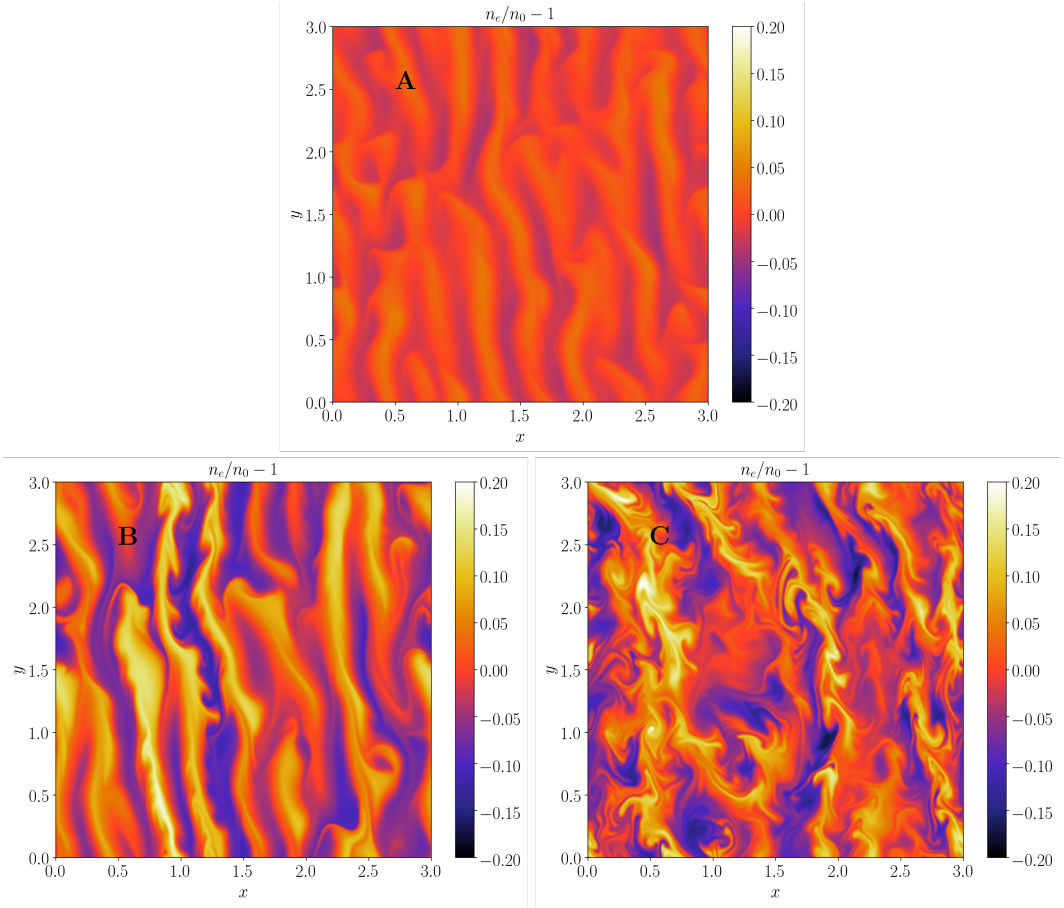

Figure 8. Evolution of δn_e. ***A:*** 1400 ion time steps. ***B:*** 1800 ion time steps. ***C:*** 3600 ion time steps

In both runs, we found that the system started deviating from number density conservation as it approached saturation. At the exponential growth phase, the difference between the total number density and the total number density at initialization was approximately $10^{-7}n_0$. Close to saturation, this number increased to approximately $10^{-5}n_0$. This ratio keeps increasing after saturation until the simulation becomes unstable. This is an expected behavior because our numerical approach was not built to be conservative. The lack of number density conservation may be related to numerical artifacts that create charge imbalances, producing electric fields that could be related to the small scale structures we see after saturation. Furthermore, we see that in both cases, $\delta \boldsymbol{E}$ increased past E_0, which is not supported by the experimental data.

5 Conclusions and Future Work

Since their discovery more than fifty years ago, we have answered numerous questions about the dynamics of Farley–Buneman instabilities. Linear theory, although limited, has produced some important verified predictions. Particle in cell simulations were able to reproduce some of the essential nonlinear local phenomena seen with rockets and radars. Using these tools together, empirical models have been constructed to improve our understanding of the Doppler signatures of these instabilities. Nevertheless, current models are unable to simulate large systems that are needed to explore non–local phe-

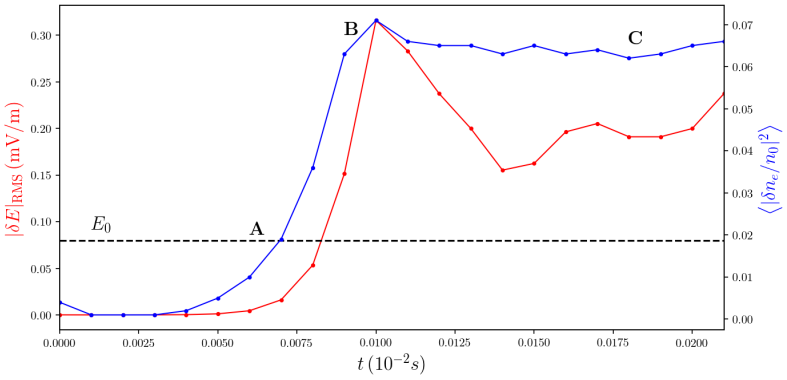

Figure 9. Evolution of δn_e and $\delta \boldsymbol{E}$ for 10000 ion time steps.

nomena. Understanding this large–scale processes are fundamental to answer some of the remaining open questions, for instance, how does density gradients affect these processes? What are the dominant wavelengths involved in Farley–Buneman turbulence? What are their Doppler signatures at off–perpendicular angles? What is the physics involved in the wave–heating processes?

In order to address these questions systematically, we need approaches that go beyond the limitations of current models and experimental techniques. Large scale spectral features, as well as the local plasma state parameters, have to be coupled by physical models. This will only be achieved with more scalable modeling and new ways to assess our empirical models.

Ion kinetic effects are needed to avoid numerical artifacts in the simulation of Farley–Buneman instabilities. However, because we are interested in non–local behavior, the high dimensionality of the kinetic equations becomes a big hurdle. Although PIC methods have been used to model kinetic behavior with great success, some of its limitations make them unsuitable for large–scale problems. For instance, due to numerical noise, is extremely difficult to resolve structures close to the amplitude of statistical noise and high energetic populations. Moreover, ionospheric plasmas require expensive Monte Carlo–simulated collisions. These limitations makes the PIC approach prohibitively expensive for non–local investigations. The goal of the present work is to build and test a small continuous hybrid simulation of Farley–Buneman instabilities to overcome some of these shortcomings.

We used a fluid isothermal model for the magnetized electrons, an electrostatic approximation for the fields, and a BGK kinetic equation for unmagnetized ions. The fluid solver was implemented by solving the corresponding diffusion–advection–reaction equation. The diffusion and reaction parts could be solved with direct integration and a Fourier spectral solver, respectively. Because of the high speed electron flows, the advective part required a characteristic based method, and for this work we used the semi–Lagrangian approach. The ion equations were split into a configuration and velocity space terms. Each of the kinetic terms were also solved using the semi–Lagrangian formalism.

Using this hybrid continuous method, we were able to resolve some of the most important features of Farley–Buneman instabilities: wave modes growing from white noise, exponential wave growth, wave turning due to thermal effects, saturation of the electric field and the density irregularities, and the primary/secondary wave dynamics. Furthermore, the simulated electric fields and density irregularities were roughly consistent with the experimental measurements from radars and rockets.

Our results are just the first steps in the direction to solve the problems related to non–local Farley–Buneman instabilities in the auroral region. Nevertheless, the tools developed here have potential for future developments. Before extending the proposed method, further analysis is needed to assess and rectify the overestimation of the perturbation electric field. Then, we need to implement thermal equations for the fluid electrons which are specially needed in the auroral region where heating can have a significant effect. Also, conservative forms of the semi–Lagrangian approach can be tested along with less oscillatory forms of interpolation. Moreover, a de–aliasing technique is required to resolve small scale structures and intermediate solutions of the electrostatic potential within each fractional step will preserve the second order accuracy of the time splitting. A more ambitious improvement would be to implement a tensor train methodology to express the phase space as tensor multiplications, reducing the effective dimensionality of the problem.

A Numerical Tests

In order to assess the numerical algorithms proposed, some tests will be presented. We will assume that the electron reaction and the diffusion steps will not require additional analysis because they are based in a direct computation and a Fourier transform, respectively. In the following numerical tests, unless explicitly mentioned, we will use the physical parameters described in Table A.1 that are representative of conditions in the auroral E–region.

Table A.1. Numerical tests: Physical parameters

Name	Symbol	Value
Background Electric field	E_0	50 mV/m
Background Magnetic field	B_0	5×10^{-5}T
Ion–neutral collision frequency	ν_{in}	2.5×10^{3}Hz
Electron and Ion temperatures	$T_e = T_i$	300K
Plasma density	N_0	$10^{10}\mathrm{m}^{-3}$

Furthermore, we will define a set of simulation parameters for the baseline case. These parameters are shown in Table A.2.

Table A.2. Numerical tests: Baseline simulation parameters

Name	Symbol	Value
Time step	dt_b	2.5×10^{-7}s
Number of grid points in each dimension	N_b	128
Lateral size of simulation box	L_b	3m

A.1 Testing ElectronSolve

The tests for the electron solver will assess the expected precision of the operator splitting approach and the advection step. Because both the physical and simulation parameters give a CFL number greater than one and periodic boundary conditions are assumed, the grid had to be extended to interpolate values outside the grid in every iter-

ation. For these tests, we will ignore ion dynamics. Therefore, contributions from $\delta \boldsymbol{E}$ will be neglected.

For the first test, we will solve 9 with constant coefficients, ignoring ion coupling. An analytical solution can be obtained by assuming a plane wave solution of the form $n = n_0 e^{(R_e - D_e|\boldsymbol{k}_w|^2)t}\cos(\boldsymbol{A}_e \cdot \boldsymbol{k}_w t - \boldsymbol{r})$, where $\boldsymbol{k}_w$ is an arbitrary wave vector, and the terms $\boldsymbol{A}_e$, D_e, and R_e can be calculated using just the linear terms of equations (9) and the values of Table A.1. With this approach, we can explore how relevant is each term in the system and whether the numerical error bound (37) holds.

The advective CFL number is given by:

$$CFL = \max(A_x, A_y)\frac{\Delta t}{\Delta x} = \max(A_x, A_y)\frac{N\Delta t}{L}, \tag{A.1}$$

where $A_{x,y}$, L, Δt, and N are the velocity components, length of grid, time step, and number of grid cells, respectively. For our purposes, $A_{x,y}$ is determined by the physical parameters of Table A.1. Consequently, to investigate the relation between simulation parameters, CFL number, and numerical precision we will focus on L, Δt, and N.

We compared the numerical solver for different simulation parameters, keeping the CFL number equal to the baseline CFL_b. Next, we modify each baseline simulation parameter so $\mathrm{CFL} = 2\mathrm{CFL}_b$ and compared the errors.

Figure (A.1) shows the results of the first set of tests. The colored texts indicate the simulation parameters in terms of the baseline parameters. Both error bounds in the top plot where calculated using equation (37). The quantity δn_{RMS} corresponds to the root mean square of the difference between the estimated and the theoretical densities. The black dots and the black line represent the errors obtained with the baseline parameters in the top and bottom plots, respectively.

The two curves of the top plot from Figure (A.1) correspond to runs with the same CFL number ($\mathrm{CFL}_b = 3.75$). We see that both errors are well bounded by the theoretical error bounds. Because the error bound for cubic splines is inversely proportional to the number of grid points, smaller errors were obtained when $N = 2N_b$. These error estimates are not significantly affected by the diffusion and reaction term, were the latter is several order of magnitude smaller than the former. As splitting theory shows, the error due to time splitting is negligible because the operators commute when their coefficients are constant. Furthermore, we see that the case when the time step and the length are doubled match almost exactly with the baseline case.

In the bottom plot from Figure (A.1) we compare the baseline case (black lines) against runs having twice the CFL number. Notice how the case were the CFL number is doubled by halving the box length shows the same errors as the case where the CFL number is doubled by doubling the time step. Doubling the number of grid points (blue line) reduces the error even if the CFL number is doubled.

The second test assess the precision of the semi–Lagrangian solver when the advection velocity is position–dependent. A 1D equation with a x dependent advection velocity will be used. The equation and its analytical solution are:

$$\frac{\partial n}{\partial t} + A(1 + f\sin(kx))\frac{\partial n}{\partial x} = 0 \tag{A.2}$$

$$n(x,t) = n\left(A\sqrt{1-f^2}t - 2\arctan\left(\frac{f + \tan(kx/2)}{\sqrt{1-f^2}}\right)\right), \tag{A.3}$$

where A, f, and k were chosen to have magnitudes representative of auroral environments. The magnitude of the advection was taken to be $A = E_0/B_0$, where the sinusoidal term emulates the perturbations caused by $\delta \boldsymbol{E}$ with f to modulate its amplitude. Notice that

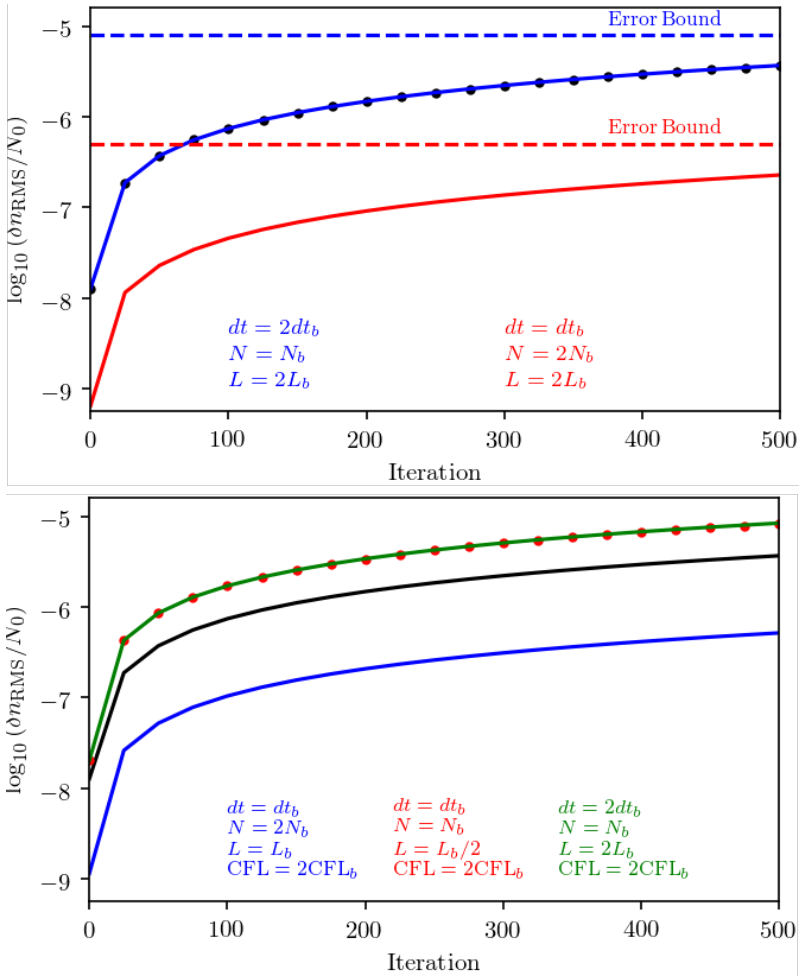

Figure A.1. Assessing precision of electron solver with constant coefficients *(Top:)* with the same CFL=CFL_b number and *(Bottom:)* between CFL_b and $2\mathrm{CFL}_b$ cases.

the solution (A.3) reduces to the constant advection case when $f = 0$. We compare the theoretical solution with two different numerical implementations of the semi–Lagrangian step: one estimating the bottom of the characteristics with the second order method outlined in section 4.3.2, and other that assumes the characteristics are position independent.

Each row of Figure (A.2) correspond to runs with different values of f. In the first column, we can see the initial density plotted in red and the distribution evaluated at subsequent times plotted in blue. In the second column, we show the errors associated with the first order (blue) and the second order (green) semi–Lagrangian steps for the iteration 5000. Finally, the last column shows the root mean square error of both implementations for 10,000 iterations.

We can see that even when $f = 0.1$, the second order method gains two orders of magnitude of precision. Furthermore, the precision of these estimates can be significantly improved by increasing the number of grid points or taking smaller time steps.

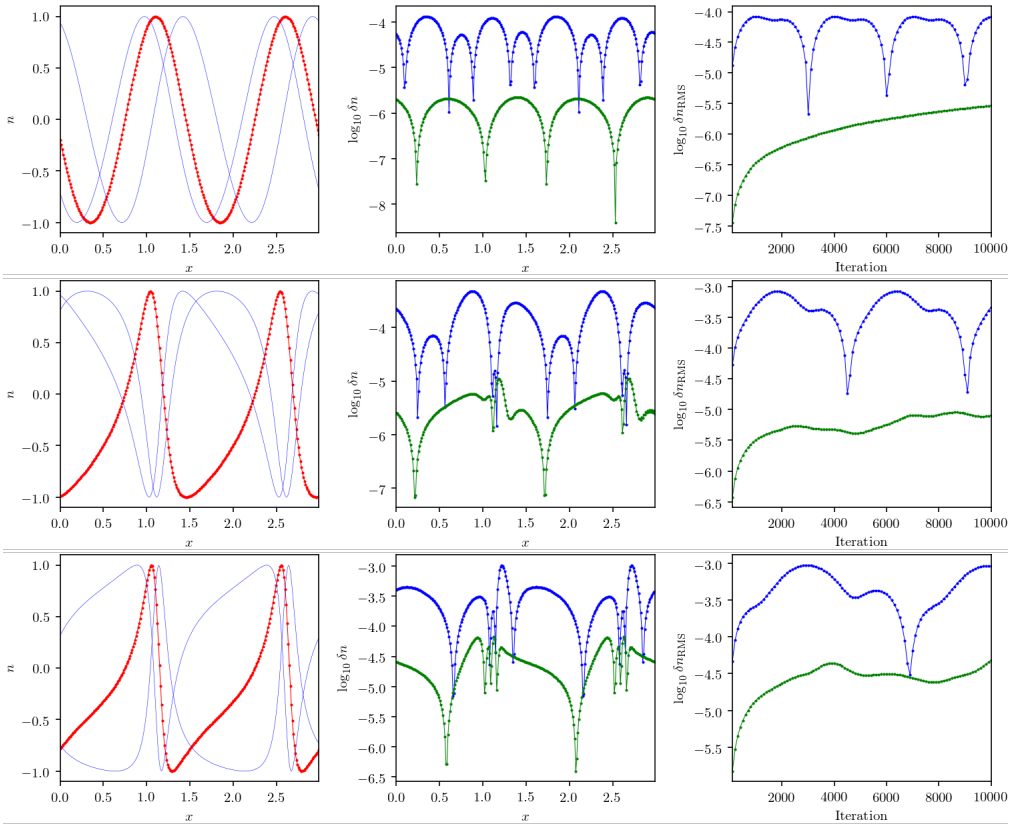

Figure A.2. Assessing precision of electron solver for 1D position–dependent advection. First, second and third column correspond to the solution at different times, errors at iteration 5000, and root mean square of the errors for 10000 iterations, respectively. *Top:* $f = 0.1$. *Middle:* $f = 0.75$. *Bottom:* $f = 0.9$.

A.2 Testing IonSolve

In order to assess the kinetic ion solver, we will use two different tests. First, we will solve the 2D×2V Vlasov equation for constant acceleration $\boldsymbol{a}$, for which the solution can be obtained analytically:

$$f(\boldsymbol{r},\boldsymbol{v},0) = g(\boldsymbol{r},\boldsymbol{v}) = \sin(2\pi k_x x)\cos(2\pi k_y y)\exp\left(-\frac{(v_x^2+v_y^2)}{2}\right) \quad \text{(A.4)}$$

$$\frac{\partial f}{\partial t} + \boldsymbol{v}\cdot\nabla f + \boldsymbol{a}\cdot\nabla_v f = 0 \quad \text{(A.5)}$$

$$f^{(teo)}(\boldsymbol{r},\boldsymbol{v},t) = g\left(\boldsymbol{r} - \boldsymbol{a}\frac{t^2}{2} - \boldsymbol{v}t, \boldsymbol{v} - \boldsymbol{a}t\right) \quad \text{(A.6)}$$

Equation (A.4) represents the initial distribution function in terms of g, equation (A.5) is the Vlasov equation with constant acceleration, and expression (A.6) is the analytical solution of (A.5). The velocity range was chosen to be $[-6v_{th}, 6v_{th}]$, the acceleration magnitude $|\boldsymbol{a}| \approx eE_0/m_i$, and the time step $dt = 10^{-4}$. This scenario emulates the evolution of the unmagnetized ion distribution function in the auroral region if electron coupling is neglected. We used a large time step to decrease the computational cost of the analysis.

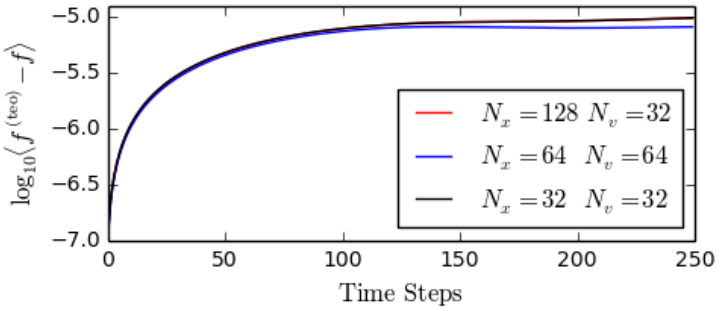

Figure A.3. Errors between theoretical and numerical solutions for constant advection in the 4D phase space and for different grid sizes.

Figure (A.3) shows the root mean square error between the theoretical and numerical estimates for different configuration and velocity grid discretizations. Notice that the errors are only slightly decreased when $N_v = 64$. Although the numerical precision will increase with smaller time steps, the computational cost of increasing the number of time steps of the kinetic solver is considerable.

For the second test, we will assess the behavior of the BGK operator qualitatively. We applied the kinetic solver to a 1D×1D collisional two–stream instability. The system was initialized with two counter–streaming electrons with Maxwellian distributions in a background of constant opposite charges and a small sinusoidal density perturbation. The electric field was calculated using a 1D Poisson spectral solver.

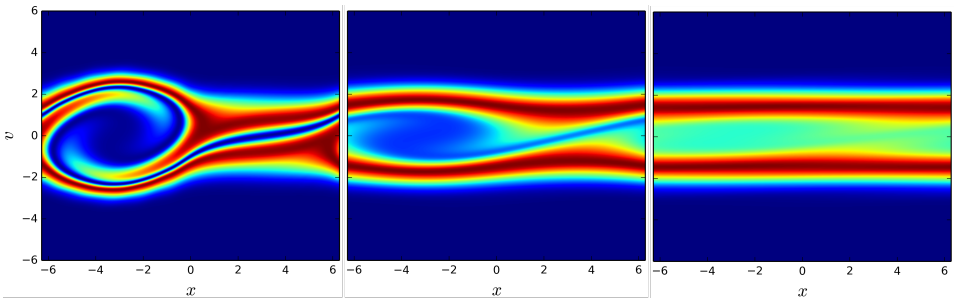

Figure A.4. 1D×1D two–stream instability simulation using the BGK-Semilagrangian scheme. *Left:* $\nu = 0$. *Middle:* $\nu = 0.1$ *Right:* $\nu = 0.2$.

Figure (A.4) shows the normalized distribution functions for different collision frequencies at the same iteration step. We can see that increasing the collision frequency thermalizes the system, raising the population of particles with zero velocity and damping the instability.

Acknowledgments

This work was supported by awards AGS-1342895 and AGS-1818216 from the National Science Foundation to Cornell University. Data were not used, nor created for this research.

References

Bahcivan, H. (2007). Plasma wave heating during extreme electric fields in the high-latitude E region. *Geophysical Research Letters*, *34*(15).

Bahcivan, H., & Cosgrove, R. (2010). On the generation of large wave parallel electric fields responsible for electron heating in the high-latitude E region. *Journal of Geophysical Research: Space Physics*, *115*(A10).

Bahcivan, H., Hysell, D., Lummerzheim, D., Larsen, M., & Pfaff, R. (2006). Observations of colocated optical and radar aurora. *Journal of Geophysical Research: Space Physics*, *111*(A12).

Cercignani, C. (2012). *The boltzmann equation and its applications* (Vol. 67). Springer.

Cheng, C., & Knorr, G. (1976). The integration of the Vlasov equation in configuration space. *Journal of Computational Physics*, *22*(3), 330–351.

Dimant, Y.S., & Oppenheim, M. (2004). Ion thermal effects on E-region instabilities: Linear theory. *Journal of Atmospheric and Solar-Terrestrial Physics*, *66*(17), 1639–1654.

Dolgov, S.V., Smirnov, A., & Tyrtyshnikov, E. (2014). Low-rank approximation in the numerical modeling of the Farley–Buneman instability in ionospheric plasma. *Journal of Computational Physics*, *263*, 268–282.

Farley, D.T. (1963). A plasma instability resulting in field-aligned irregularities in the ionosphere. *Journal of Geophysical Research*, *68*(22), 6083–6097.

Farley, D.T. (2009). The equatorial E-region and its plasma instabilities: A tutorial. *Ann. Geophys*, *27*(4), 1509–1520.

Fejer, B.G., Providakes, J., & Farley, D. (1984). Theory of plasma waves in the auroral E region. *Journal of Geophysical Research: Space Physics*, *89*(A9), 7487–7494.

Filbet, F., Sonnendrücker, E., & Bertrand, P. (2001). Conservative numerical schemes for the Vlasov equation. *Journal of Computational Physics*, *172*(1), 166–187.

Fuller-Rowell, T.J., Codrescu, M., Moffett, R., & Quegan, S. (1994). Response of the thermosphere and ionosphere to geomagnetic storms. *Journal of Geophysical Research: Space Physics*, *99*(A3), 3893–3914.

Glowinski, R., Osher, S., & Yin, W. (2017). *Splitting methods in communication, imaging, science, and engineering*. Springer.

Groppi, M., Russo, G., & Stracquadanio, G. (2016). High order semi–Lagrangian methods for the BGK equation. *Communications in Mathematical Sciences*, *14*(2), 389–414.

Hammett, G.W., & Perkins, F. (1990). Fluid moment models for Landau damping with application to the ion-temperature-gradient instability. *Physical review letters*, *64*(25), 3019.

Hassan, E., Horton, W., Smolyakov, A., Hatch, D., & Litt, S. (2015). Multiscale equatorial electrojet turbulence: Baseline 2D model. *Journal of Geophysical Research: Space Physics*, *120*(2), 1460–1477.

Hesthaven, J.S. (2017). *Numerical methods for conservation laws: From analysis to algorithms*. SIAM.

Hundsdorfer, W., & Verwer, J. (2013). *Numerical solution of time-dependent advection–diffusion–reaction equations* (Vol. 33). Springer.

Hysell, D.L. (2015). The radar aurora. In *Auroral dynamics and space weather* (pp. 191–209). John Wiley & Sons.

Hysell, D.L., Aveiro, H., & Chau, J. (2013). Ionospheric irregularities: frontiers. *Geophys. Monogr. Ser*, *201*, 217–240.

Janhunen, P. (1994). Perpendicular particle simulation of the E region Farley–Buneman instability. *Journal of Geophysical Research: Space Physics*, *99*(A6), 11461–11473.

Kovalev, D.V., Smirnov, A., & Dimant, Y. (2008). Modeling of the Farley–Buneman instability in the E-region ionosphere: A new hybrid approach. *Annales Geophysicae*, *26*(9), 2853.

Kovalev, D.V., Smirnov, A., & Dimant, Y. (2009). Simulations of the nonlinear stage of Farley–Buneman instability with allowance for electron thermal effects. *Plasma Physics Reports*, *35*(7), 603–610.

Lanser, D., & Verwer, J. (1999). Analysis of operator splitting for advection–diffusion–reaction problems from air pollution modelling. *Journal of Computational and Applied Mathematics*, *111*(1-2), 201–216.

Liboff, R.L. (2003). *Kinetic theory: Classical, quantum, and relativistic descriptions.* Springer.

Machida, S., & Goertz, C. (1988). Computer simulation of the Farley–Buneman instability and anomalous electron heating in the auroral ionosphere. *Journal of Geophysical Research: Space Physics*, *93*(A9), 9993–10000.

Newman, A.L., & Ott, E. (1981). Nonlinear simulations of type 1 irregularities in the equatorial electrojet. *Journal of Geophysical Research: Space Physics*, *86*(A8), 6879–6891.

Oppenheim, M., & Dimant, Y. (2004). Ion thermal effects on E–region instabilities: 2D kinetic simulations. *Journal of Atmospheric and Solar-Terrestrial Physics*, *66*(17), 1655–1668.

Oppenheim, M., & Dimant, Y. (2013). Kinetic simulations of 3D Farley–Buneman turbulence and anomalous electron heating. *Journal of Geophysical Research: Space Physics*, *118*(3), 1306–1318.

Oppenheim, M., Dimant, Y., & Dyrud, L. (2008). Large–scale simulations of 2D fully kinetic Farley–Buneman turbulence. *Annales Geophysicae*, *26*(3), 543–553.

Oppenheim, M., Otani, N., & Ronchi, C. (1996). Saturation of the Farley–Buneman instability via nonlinear electron ExB drifts. *Journal of Geophysical Research: Space Physics*, *101*(A8), 17273–17286.

Qiu, J., & Christlieb, A. (2010). A conservative high order semi–Lagrangian WENO method for the Vlasov equation. *Journal of Computational Physics*, *229*(4), 1130–1149.

Quarteroni, A., & Valli, A. (2008). *Numerical approximation of partial differential equations* (Vol. 23). Springer.

Robert, A. (1981). A stable numerical integration scheme for the primitive meteorological equations. *Atmosphere-Ocean*, *19*(1), 35–46.

Rojas, E.L., Hysell, D., & Munk, J. (2018). Assessing ionospheric convection estimates from coherent scatter from the radio aurora. *Radio Science*, *53*(12), 1481–1491.

Rojas, E.L., Young, M., & Hysell, D. (2016). Phase speed saturation of Farley–Buneman waves due to stochastic, self–induced fluctuations in the background flow. *Journal of Geophysical Research: Space Physics*, *121*(6), 5785–5793.

Sahr, J.D., & Fejer, B. (1996). Auroral electrojet plasma irregularity theory and experiment: A critical review of present understanding and future directions. *Journal of Geophysical Research: Space Physics*, *101*(A12), 26893–26909.

Schmidt, M.J., & Gary, S. (1973). Density gradients and the Farley–Buneman instability. *Journal of Geophysical Research*, *78*(34), 8261–8265.

Schunk, R., & Nagy, A. (2009). *Ionospheres: physics, plasma physics, and chemistry.* Cambridge University Press.

Sonnendrücker, E., Roche, J., Bertrand, P., & Ghizzo, A. (1999). The semi–Lagrangian method for the numerical resolution of the Vlasov equation. *Journal of Computational Physics*, *149*(2), 201–220.

St.Maurice, J.P. (1990). Electron heating by plasma waves in the high latitude E–region and related effects: Theory. *Advances in Space Research*, *10*(6), 239–249.

Strang, G. (1968). On the construction and comparison of difference schemes. *SIAM Journal on Numerical Analysis*, *5*(3), 506–517.

Wiltberger, M., Merkin, V., Zhang, B., Toffoletto, F., Oppenheim, M., Wang, W., ... Sitnov, M. (2017). Effects of electrojet turbulence on a magnetosphere-ionosphere simulation of a geomagnetic storm. *Journal of Geophysical Research: Space Physics*, *122*(5), 5008–5027.